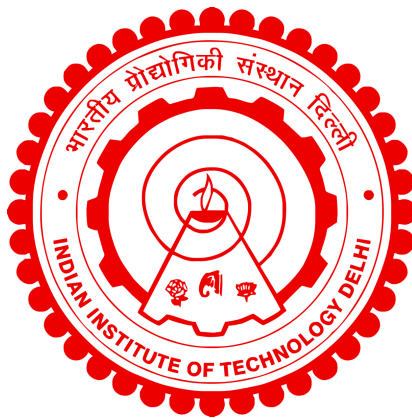


**INVESTIGATIONS ON TRANSIENT FLOW IN
DRAFT TUBE OF A FRANCIS TURBINE
DURING LOAD VARIATION**

FAIZ AZHAR MASOODI



**DEPARTMENT OF ENERGY SCIENCE AND
ENGINEERING**

INDIAN INSTITUTE OF TECHNOLOGY DELHI

AUGUST 2025

© Indian Institute of Technology Delhi (IITD), New Delhi, 2025

**INVESTIGATIONS ON TRANSIENT FLOW IN
DRAFT TUBE OF A FRANCIS TURBINE
DURING LOAD VARIATION**

by

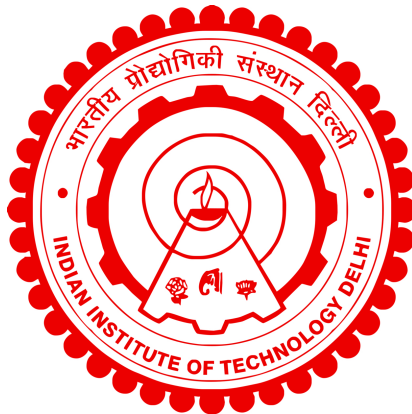
FAIZ AZHAR MASOODI

Department of Energy Science and Engineering

Submitted

in partial fulfillment of the requirements of the degree of Doctor of Philosophy

to the



**INDIAN INSTITUTE OF TECHNOLOGY
DELHI**

AUGUST 2025

Dedicated to

*The abiding memory of my beloved grandfather - late
Saif-Ud-Din Saifi, my first teacher and the most
affectionate person I have ever met.*

*Mom and Dad.
At their feet lies my existence; in their service my life
finds purpose.*

Certificate

This is to certify that the thesis entitled “**Investigations on Transient Flow in Draft Tube of a Francis Turbine During Load Variation**”, submitted by **Mr. Faiz Azhar Masoodi** to the Indian Institute of Technology Delhi, for the award of the degree of **Doctor of Philosophy** in Energy Science and Engineering, is a record of the original, bona fide research work carried out by him under my supervision and guidance. The thesis has reached the standards fulfilling the requirements of the regulations related to the award of the degree.

The results contained in this thesis have not been submitted in part or in full to any other University or Institute for the award of any degree or diploma to the best of my knowledge.

Prof. Rahul Goyal

Associate Professor

Department of Energy Science and Engineering,

Indian Institute of Technology Delhi.

Acknowledgement

“I can no other answer make but thanks,
And thanks; and ever thanks”

– William Shakespeare, *The Twelfth Night*.

Redemption of all joy and reward is founded on a simple and beautiful emotion – gratitude. While it is never possible to recompense for the acts of goodness and kindness we are often times meted, humble strokes of my pen intend to express the awe and admiration I deeply feel as I arrive at an important milestone in career, the completion of doctoral education. I open this letter of gratitude with ‘Al-hamdu-lillah’, an Arabic phrase which translates to ‘all praise is due to Almighty God’. Indeed, no amount of expression suffices to thank God Almighty for this beautiful life and the abundant and countless blessings that accompany.

Prof. Rahul Goyal, my researcher supervisor, remains an exemplar of diligence, persistence and fortitude besides being a teacher of extraordinary prowess. The fortuity of PhD studentship under his guidance enabled me to realize the best of my capability in research and beyond. I have tremendously benefitted from the invigorating and impactful technical discussions I have had with him throughout my doctoral study. Besides, Prof. Goyal has always laid on offer the affection and warmth much required by an early stage researcher. I document my sincere gratitude to him.

I am grateful to the appointed members of my research assessment panel at Indian Institute of Technology, Delhi. Prof. K.A. Subramanian, Prof. P.M.V. Subbarao and Prof. S.K. Tyagi have made valuable suggestions during the progress review meetings. I am highly thankful to them. I would also like to thank Dr. Saeed Salehi, our collaborator at Chalmers University, Sweden, for his invaluable inputs. I am also thankful to the high-performance computing centre at Indian Institute of Technology, Delhi for provision of computational resource to perform my investigations. I express my heartfelt gratitude to the clerical and administrative staff who have been a part of my academic journey. I would particularly like to thank Mrs. Poonam Negi who promptly acceded to all my requests at the postgraduate academic section.

I was lucky to have wonderful colleagues at Hydro and Wind Power Laboratory, Department of Energy Science and Engineering. I found affectionate friends in Pallav, Dishant, Vishnu, Ashwin, Vineeth, Aditya, Dr. Ratnadeep and Dr. Sonu. Our friendship has only grown over time to unite us into a family. I am grateful to them for the support and respect they have always shown.

At the outset of my doctoral education, I met two kind and lovely fellow students, Omar and Saqib. Little did I know then that this acquaintance will go on to be amongst the most cherished. Today, many years after, I would like to call them family. I express my deepest gratitude for their exemplary love, support and respect. While it is not possible to make every individual mention, I am grateful to all other beloved friends at the Indian Institute of Technology, Delhi for their comforting kinship.

Of all I have, my parents remain the dearest. I would like to express boundless gratitude to my mother, Tahira Masoodi. Her incessant prayers have powered my journey through the PhD program. Her love remains unrequitable. My father, Dr. Muhammad Azhar Masoodi, has been a mentor, a role model, a friend and a source of constant support, encouragement and affection in all that I have ever endeavoured. I remain measurelessly thankful to him. I am also thankful to my brother Dr. Faisal Azhar Masoodi, his lovely wife Ifat Masoodi, and their beautiful kids Jawad Faheem and Muhammad Ibrahim for nourishing me with care and affection.

I am filled with fond remembrances of my grandfather Saif -Ud - Din Saifi; it was his earnest desire to see me pursue doctoral education and serve as an academic. Much of my psychological drives are shaped by his affection and upbringing. I am grateful to him, forever. I am highly thankful to my uncle Farooq Ahmad Masoodi, who taught me elementary physics and kindled in me a profound interest for science.

I arrived in Delhi five years ago with a dream in eyes and faith in heart. The city and its warm environment have nourished the dream and strengthened the faith. Thank you, Delhi - for the moments of joy, and those of sorrow, and those of bustle, and those of silence!

Faiz Azhar Masoodi

21/08/2025

Abstract

Off-design and transient operations of hydraulic turbines is contemporarily frequented for balancing the grid power intermittence introduced by variable renewable energy. Steady state operation is characterized by a constant discharge and varied conditions of load such as the best efficiency point, part load, deep part load, high load and full load. Load change, and start/stop events are the regimes of transient operation and involve a time varying flow rate. An adverse consequence of off-design/transient turbine operations is development of vortex breakdown phenomenon. Vortex breakdown in draft tubes manifests as a rotating vortex rope at part load operation and enlarged vortex core at high load operation. Development of vortex breakdown causes a complete disorganization of the flow with development of unfavourable pressure fluctuation leading to loss of turbine efficiency.

This thesis encapsulates thorough numerical investigations on the formation and elimination of the enlarged vortex core and rotating vortex rope consequent to load changes on the turbine. Steady state turbine operation at best efficiency point, high load and part load conditions as well as transient operations between these operating points are simulated. Initially, a detailed assessment of the applicability of URANS-based standard $k - \epsilon$ and SST $k - \omega$ turbulence models for the characterization of a part load vortex rope is carried out. Simulations are performed at part load using the commercially available ANSYS CFX software. Obtained axial and radial velocity fields are compared with results from the experiment. A detailed spectral analysis is carried out using Fast Fourier Transforms to identify the dominant frequencies of pressure fluctuation in numerical and experimental data. A mismatch between experiment and simulation is identified and quantified to evaluate the utility of URANS models for investigations on vortex breakdown. It is discerned that more advanced turbulence models are required for an accurate flow field prediction.

Subsequent simulations of steady state turbine operation at best efficiency point, high load and part load, as well as transient operations between these operating points, are conducted using OpenFOAM open-source software. Turbulence closure is attained using the scale adaptive simulations - shear stress transport turbulence model. Dynamic meshing based on a Laplacian smoothing scheme is used to account for mesh deformation arising from guide vane motion during load change.

The pressure and velocity fields have been determined and analyzed to elucidate the physics of vortex breakdown, the phenomenon underlying the formation of the enlarged vortex core and rotating vortex rope. At best efficiency point, a close agreement between numerical and experimental velocity profiles is seen. However, at high load and part load, while the numerical results agree satisfactorily with experiment toward the peripheral region, a slightly increased deviation is seen in the central region due to the presence of vortex breakdown.

Vortex breakdown in the draft tube occurs due to exceedance of the swirl magnitude beyond a critical value. Transient operations of the turbine from best efficiency point to off-design conditions lead to an exceeded magnitude of swirl in the flow exiting the runner. Consequently, vortex breakdown occurs in the draft tube causing an unusual flow pattern. The vortex core significantly swells up toward high load. A central axial flow stagnation commences centrally near 50% of the transient sequence duration. Subsequently, flow is separated into a nearly stagnant, expanded central vortex core, and a high-speed outflow surrounding it. A steep axial velocity change is observed radially across the interface of outflow and vortex core earmarking strong shear layers, which roll up to form a compact spiral structure. Flow reversals within the enlarged vortex core are seen to be intermittent. Reverse transition from high load to best efficiency point results in a gradual reorganization of the velocity field, purging main features of the vortex breakdown such as flow reversals and stagnation, within 50% of the time of load change. Onward, the flow is gradually restored to a form characteristic of the best efficiency point.

In the best efficiency point to part load transient sequence the changes in velocity field are noticeable after about 30% of the time of transient operation has elapsed. VB commences with a central flow stagnation in the draft tube. The flow separates about a stagnation point leading to development of a stagnation region that dilates radially in time. Post 50% of the transient operation intermittent flow reversals are observed within the stagnation region. The flow at PL is stabilized after completion of the transient sequence. A wavy boundary of the stagnation region earmarks the strong radial gradients of axial velocity representing strong interfacial shear layers between the stagnation region and surrounding outflow. The shear layers roll up leading to formation of rotating vortex rope. The flow morphology depicts a spiral type vortex breakdown.

सारांश

हाइड्रोलिक टरबाइन का ऑफ-डिज़ाइन और क्षणिक (transient) संचालन आजकल अक्सर उस ग्रिड पावर अस्थिरता को संतुलित करने के लिए किया जाता है, जो परिवर्तनीय नवीकरणीय ऊर्जा स्रोतों से उत्पन्न होती है। स्थिर अवस्था (steady state) संचालन को एक स्थिर प्रवाह दर और विभिन्न भार स्थितियों – जैसे कि सर्वश्रेष्ठ दक्षता बिंदु, आंशिक भार, गहरे आंशिक भार, उच्च भार और पूर्ण भार – से परिभाषित किया जाता है। भार परिवर्तन तथा स्टार्ट/स्टॉप जैसी घटनाएँ क्षणिक संचालन के अंतर्गत आती हैं, जहाँ प्रवाह दर समय के साथ बदलती है। ऑफ-डिज़ाइन/क्षणिक टरबाइन संचालन का एक प्रतिकूल परिणाम वॉर्टेक्स ब्रेकडाउन (vortex breakdown) की उत्पत्ति है। ड्राफ्ट ट्यूब में वॉर्टेक्स ब्रेकडाउन आंशिक भार पर घूमते हुए वॉर्टेक्स रोप (rotating vortex rope) और उच्च भार पर विस्तारित वॉर्टेक्स कोर के रूप में प्रकट होता है। वॉर्टेक्स ब्रेकडाउन का विकास प्रवाह को असंगठित कर देता है और अवांछित दाब उतार-चढ़ाव पैदा करता है, जिससे टरबाइन दक्षता घट जाती है।

यह शोध प्रबंध टरबाइन पर भार परिवर्तन के परिणामस्वरूप विकसित होने वाले विस्तारित वॉर्टेक्स कोर और घूमते वॉर्टेक्स रोप की उत्पत्ति एवं उनके निराकरण पर गहन संख्यात्मक जाँच प्रस्तुत करता है। स्थिर अवस्था में टरबाइन संचालन को सर्वश्रेष्ठ दक्षता बिंदु, उच्च भार और आंशिक भार स्थितियों पर तथा इन बिंदुओं के बीच क्षणिक संचालन को भी सिमुलेट किया गया है। प्रारंभ में, आंशिक भार वॉर्टेक्स रोप के लक्षण निर्धारण हेतु URANS आधारित मानक $k-\epsilon$ और SST $k-\omega$ टर्बुलेंस मॉडल की प्रयोज्यता का विस्तृत मूल्यांकन किया गया। आंशिक भार पर सिमुलेशन ANSYS CFX वाणिज्यिक सॉफ्टवेयर का उपयोग करके किए गए और प्राप्त अक्षीय व रेडियल वेग क्षेत्रों की तुलना प्रायोगिक परिणामों से की गई। प्रेशर उतार-चढ़ाव की प्रमुख आवृत्तियों को पहचानने हेतु FFT आधारित विस्तृत स्पेक्ट्रल विश्लेषण किया गया। प्रयोग और सिमुलेशन के बीच अंतर का मूल्यांकन कर यह स्पष्ट किया गया कि वॉर्टेक्स ब्रेकडाउन की सटीक भविष्यवाणी के लिए और अधिक उन्नत टर्बुलेंस मॉडलों की आवश्यकता है।

इसके बाद, स्थिर अवस्था (सर्वश्रेष्ठ दक्षता बिंदु, उच्च भार, आंशिक भार) और इन अवस्थाओं के बीच क्षणिक संचालन के सिमुलेशन OpenFOAM ओपन-सोर्स सॉफ्टवेयर में किए गए। इसमें Scale Adaptive Simulation – Shear Stress Transport (SAS-SST) टर्बुलेंस मॉडल का उपयोग किया गया और लोड परिवर्तन के दौरान गाइड वेन की गति से उत्पन्न जाल (mesh) विकृति को समायोजित करने के लिए Laplacian smoothing आधारित डायनामिक मेसिंग का उपयोग हुआ। दबाव और वेग क्षेत्रों का विश्लेषण कर वॉर्टेक्स ब्रेकडाउन की भौतिकी, विशेषकर विस्तारित वॉर्टेक्स कोर और घूमते वॉर्टेक्स रोप की उत्पत्ति, स्पष्ट की गई। सर्वश्रेष्ठ दक्षता बिंदु पर संख्यात्मक और प्रायोगिक वेग प्रोफाइल में निकटतम सामंजस्य पाया गया। किंतु उच्च और

आंशिक भार पर, परिधीय क्षेत्र में तो परिणाम संतोषजनक थे, परंतु केंद्रीय क्षेत्र में वॉर्टेक्स ब्रेकडाउन की उपस्थिति के कारण कुछ विचलन पाया गया।

ड्राफ्ट ट्यूब में वॉर्टेक्स ब्रेकडाउन तब होता है जब स्वर्ल की परिमाण (swirl magnitude) एक निर्णायक सीमा से अधिक हो जाता है। टरबाइन का क्षणिक संचालन, सर्वश्रेष्ठ दक्षता बिंदु से ऑफ-डिज़ाइन स्थितियों की ओर जाते समय, रनर से निकलने वाले प्रवाह में स्वर्ल को अत्यधिक बढ़ा देता है। फलस्वरूप, ड्राफ्ट ट्यूब में वॉर्टेक्स ब्रेकडाउन उत्पन्न होता है और असामान्य प्रवाह संरचना बनती है। उच्च भार पर वॉर्टेक्स कोर का आकार काफी बढ़ जाता है। लगभग 50% क्षणिक क्रम की अवधि में केंद्रीय अक्षीय प्रवाह स्थगन (stagnation) आरंभ हो जाता है। इसके बाद प्रवाह एक लगभग स्थिर, विस्तारित केंद्रीय वॉर्टेक्स कोर और उसके चारों ओर उच्च वेग वाले आउटफ़्लो में विभाजित हो जाता है। इस इंटरफ़ेस पर तेज अक्षीय वेग परिवर्तन देखा गया, जो प्रबल शियर लेयर्स बनाता है और अंततः एक कॉम्पैक्ट सर्पिल संरचना में लिपट जाता है। विस्तारित वॉर्टेक्स कोर के भीतर प्रवाह का उलटना (flow reversal) रुक-रुक कर होता है। उच्च भार से सर्वश्रेष्ठ दक्षता बिंदु की ओर उलटे संक्रमण के दौरान लगभग 50% समय में प्रवाह क्षेत्र पुनर्गठित हो जाता है और वॉर्टेक्स ब्रेकडाउन की मुख्य विशेषताएँ जैसे प्रवाह उलटना और स्थगन समाप्त हो जाती हैं। इसके बाद प्रवाह धीरे-धीरे सर्वश्रेष्ठ दक्षता बिंदु की विशेषता वाले रूप में लौट आता है।

सर्वश्रेष्ठ दक्षता बिंदु से आंशिक भार की क्षणिक क्रमावली में, प्रवाह वेग क्षेत्र में परिवर्तन लगभग 30% समय बीत जाने के बाद स्पष्ट दिखाई देते हैं। VB ड्राफ्ट ट्यूब में केंद्रीय प्रवाह स्थगन से आरंभ होता है। प्रवाह एक स्थगन बिंदु के चारों ओर विभाजित हो जाता है, जिससे एक स्थगन क्षेत्र विकसित होता है जो समय के साथ रेडियल रूप से फैलता है। 50% समय के बाद इस स्थगन क्षेत्र में रुक-रुक कर प्रवाह उलटना देखा गया। आंशिक भार पर प्रवाह क्षणिक क्रम पूरा होने के बाद स्थिर हो जाता है। स्थगन क्षेत्र की लहरदार सीमा, अक्षीय वेग के तीव्र रेडियल प्रवणताओं को दर्शाती है, जो स्थगन क्षेत्र और उसके चारों ओर के आउटफ़्लो के बीच मजबूत इंटरफ़ेस शियर लेयर का प्रतिनिधित्व करती है। ये शियर लेयर्स लिपट कर घूमते वॉर्टेक्स रोप का निर्माण करती हैं। प्रवाह संरचना सर्पिल प्रकार के वॉर्टेक्स ब्रेकडाउन को प्रदर्शित करती है।

Contents

Certificate	i
Acknowledgement	iii
Abstract	v
सारांश	vii
Contents	ix
List of Figures	xiii
List of Tables	xxi
Abbreviations	xxiii
Symbols	xxv
1 Introduction	1
1.1 Hydraulic turbines	2
1.2 Vortex breakdown in hydraulic turbines	7
2 Review of Literature	11
2.1 Experimental investigations	13
2.1.1 Flow characterization	13
2.1.2 Spectral analysis	23
2.1.3 Cavitation effects in vortex ropes	26
2.2 Numerical investigations	39
2.2.1 Flow field investigations	41
2.2.2 A note on turbulence modelling	51
2.3 Formation mechanism of vortex rope	54

2.4	Research gaps	65
2.5	Research objectives	66
3	Computational Methodology	67
3.1	Governing equations	67
3.2	Reynolds-averaged Navier-Stokes (RANS) approach	69
3.2.1	k - ϵ turbulence model	71
3.2.2	k - ω turbulence model	72
3.2.3	Shear stress transport (SST) k - ω turbulence model	72
3.3	Large eddy simulations (LES)	73
3.4	Hybrid or bridging turbulence models	79
3.4.1	Shear stress transport – Scale adaptive simulations (SST-SAS) model	79
3.4.2	Partially-averaged Navier-Stokes (PANS) model	80
3.5	Near wall modelling	83
3.6	Test case	84
3.7	Discretization and numerical schemes	87
3.8	The computational mesh	90
3.9	Simulated operating conditions	94
3.10	Boundary conditions	95
4	Steady State Operations	97
4.1	Capability assessment of URANS models	98
4.1.1	Methodology of computation	98
4.1.2	Velocity prediction	100
4.1.3	Pressure prediction	105
4.2	Steady state operation	109
4.2.1	Case validation and velocity profiles	109
4.2.2	Draft tube velocity field	117
4.3	PANS simulations	123
4.4	Proper orthogonal decomposition	128
4.4.1	Background	128
4.4.2	Cumulative energy	130
4.4.3	Frequency content	131
4.4.4	Coherent structures	135
4.5	Summary	140
5	Transient Operations	141
5.1	Swirl number	142
5.2	Velocity field	144
5.2.1	BEP -HL load change	144
5.2.2	HL - BEP load change	151

5.2.3	BEP - PL load change	163
5.3	Pressure field	170
5.3.1	BEP - HL load change	170
5.3.2	HL - BEP load change	174
5.4	Flow visualizations	178
5.4.1	BEP - HL load change	178
5.4.2	HL - BEP load change	180
5.4.3	BEP - PL load change	183
5.5	Vorticity distribution	185
5.6	PANS simulations	188
5.7	Computational cost	196
5.8	Summary	197
6	Conclusions	199
6.1	Summary	199
6.1.1	Steady state operation	200
6.1.2	Transient operation	203
6.2	Future scope of work	205
	Bibliography	209
	List of Publications	235
	Curriculum Vitae	237

List of Figures

1.1	A schematic representation of the water cycle[3]	2
1.2	Categorization of turbines for selection based on specific speed and head[6]	4
1.3	A schematic representation of the working of a hydroelectric power plant[7]	5
1.4	Components of a Francis turbine	6
1.5	Hill chart of a model high head Francis turbine[8]	6
1.6	Vector diagrams of velocity at outlet of a Francis runner under a) PL b) BEP c) HL operations[5]. U is the runner velocity, V the absolute flow velocity, and W the relative velocity of flow with respect to the runner. V_a and V_t are axial and circumferential velocity components, respectively.	8
1.7	Visuals of RVR (left) and EVC (right) in the draft tube[6]	9
2.1	Spiral vortex core enveloping the stagnation region at PL turbine operation[51]	14
2.2	The Francis 99 model test section showing placement of PIV system and pressure sensors: a) top view b) side view[13]	15
2.3	Contour plots of absolute flow velocity (V) in the draft tube at a) BEP operation b) PL operation[13]	16
2.4	Mean axial and radial velocities at two cross-sections (line 1 and line 2) of the draft tube cone for 20 repetitions[13]	16
2.5	Salient locations of measurement in the U9 draft tube. Red dots indicate pressure sensors[54]. Section I-III are the LDA measurement sections. a, b, c, and d represent the circumferential alignment of pressure and velocity measurements	17
2.6	Averaged axial (U^*) and tangential velocity (V^*) profiles at salient sections of measurement during BEP operation[54]	17
2.7	Time evolution of normalized velocities in the draft tube during PL operation: a) radial (U^*) and b) axial (V^*) velocities[13].	19
2.8	Averaged axial (U^*) and tangential velocity (V^*) profiles at salient sections of measurement during PL operation[54]	20

2.9	Visual of the RVR obtained using air injection (left) and a schematic representation of the RVR (right)[54]. ω_1 and rRVR are the angular velocity and radius of precession respectively. ω_2 is the angular velocity of self-rotation of the vortex	22
2.10	Axial velocity phase averaged with respect to RVR frequency represented by a contour plot[54]	22
2.11	Tangential velocity phase averaged with respect to RVR frequency represented by a contour plot[54]	23
2.12	Spectrograms of pressure-time signals acquired in the draft tube cone during a) BEP-PL load change and b) PL-BEP load change acceptance[13]. Black solid line represents the time variation of GV angle scaled on top-right y-axis	24
2.13	Spectrograms of a) plunging and b) rotating modes of RVR acquired during PL-BEP load change[13]. Black solid line represents the time variation of GV angle scaled on top-right y-axis	25
2.14	Spectrograms of a) plunging and b) rotating modes of RVR acquired during BEP-PL load change[13]. Black solid line represents the time variation of GV angle scaled on top-right y-axis	25
2.15	BEP-PL load change effected appearance of rotating and plunging components of the RVR in the draft tube cone[13]. Time evolution of pressure (left) radial velocity (centre) and axial velocity (right) amplitudes in RVR frequency is shown. Blue solid line represents the time variation of GV angle scaled on top-right y-axis. Black and dashed solid lines indicate appearance of the plunging and rotating components of RVR, respectively.	26
2.16	Representation of pressure fluctuation amplitudes against frequency through a waterfall diagram at cone downstream (left) and cone upstream (right) locations[47]	29
2.17	Plot of frequency (red) and amplitude (green) of pressure fluctuation against cavitation number[47]	29
2.18	Fast Fourier transform of the pressure coefficient at a point on draft tube wall near inlet ($Q = 0.82.Q_{BEP}$)[75]	31
2.19	Short time Fourier transform (STFT) of the pressure coefficient at a point on draft tube wall near inlet for three cavitation numbers σ a) 0.26 b) 0.20 c) 0.15 ($Q = 0.82.Q_{BEP}$) [75]	32
2.20	Stability diagram identifying unstable operating regimes involving upper part load (UPL) instability in a model Francis turbine[75]	33
2.21	Visual illustration of volume fluctuation related to upper part load (UPL) instability seen in a cavitating vortex rope near runner hub ($Q = 0.87Q_{BEP}$, Cavitation number = 0.06)[81]	34
2.22	Different patterns of vortex ropes seen in a draft tube under various operating regimes[85]	36

2.23	Distribution of different patterns of vortex ropes seen in a draft tube as per operating regimes[85]	37
2.24	Root mean square values of pressure in draft tube (PDT1), penstock (PP2) and spiral casing (PSC1), and shaft displacement (DT1) over the range of PL operation[12]	38
2.25	Time-frequency diagram of pressure in the draft tube cone (PDT1) and spiral casing (PSC1)[12]	38
2.26	A plot of dominant frequencies over the operating range of the turbines[12]	38
2.27	Spanwise profiles of axial velocity at different instants in course of BEP-PL load change[26]	42
2.28	Contour plot showing time evolution of axial velocity in the draft tube cone at a measuring place near draft tube inlet a) experimental data b) numerical data[26]	42
2.29	Time evolution of axial velocity at four different radial positions[26]	43
2.30	Pressure iso-surfaces for RVR visualization, generated using DES model at PL (left), BEP (centre) and HL (right) conditions[121]	44
2.31	Spanwise profiles of axial velocity generated in the draft tube cone at upstream (left) and downstream (right) locations during BEP operation[121]	44
2.32	Spanwise profiles of axial velocity generated in the draft tube cone at upstream (left) and downstream (right) locations during PL operation[121]	45
2.33	Spanwise distribution of axial (V) and radial (U) velocities generated in the draft tube cone at a) upstream and b) downstream locations during BEP operation [122]	46
2.34	Spanwise distribution of axial (V) and radial (U) velocities generated in the draft tube cone at a) upstream and b) downstream locations during PL operation[122]	46
2.35	Spanwise profiles of radial velocity generated in the draft tube cone at upstream (left) and downstream (right) locations during BEP operation[121]	47
2.36	Spanwise profiles of radial velocity generated in the draft tube cone at upstream (left) and downstream (right) locations during PL operation [121]	47
2.37	Distribution of normalized tangential velocity across draft tube cone radius near inlet during BEP operation[119].	48
2.38	Distribution of normalized tangential velocity across draft tube cone radius near inlet during PL operation[119].	48
2.39	PL pressure fluctuation in the draft tube cone captured using various turbulence models[128]. Left and right diagrams correspond to two different locations of pressure measurement on the draft tube	51
2.40	A vortex tube generally used for experimentation on VB[21]	55

2.41	Double helix type (top), spiral type (middle) and bubble type VBs [21]	56
2.42	Sketch of a spiral rotating vortex representing the periodic motion in a vortex whistle[163]	58
2.43	Variation of swirl number (left ordinate) and maximum amplitude of precession frequency of RVR (right ordinate) with discharge normalized by BEP flow rate[168]	60
2.44	Formation of an axisymmetric (bubble type) VB downstream of a GV system by core swelling[37]	61
2.45	Spanwise evolution of a) absolute, b) axial and c) axial velocities characterizing VB caused by BEP-PL load change[13]. Load change from BEP is initiated at 8.65s and PL is reached at 11.15s	63
2.46	Streamlines generated from averaged steady solution of the transient (PL-BEP) flow condition at various instants [41]. Twenty repetitions of measurement are used for averaging.	64
3.1	Geometry of the investigated test case	86
3.2	Test section of the experimental rig and numerical test case	87
3.3	Pictures of the mesh created in different parts of the domain	92
3.4	Pictures of the unmorphed (BEP) and morphed (HL) mesh near guide vanes	94
4.1	Visuals of the computational mesh	100
4.2	Numerical and experimental profiles of mean axial velocity on measurement line 1 at PL	102
4.3	Numerical and experimental profiles of axial velocity on measurement line 2 at PL	102
4.4	Deviation of numerical axial velocity data from experiment along measurement line 1 at PL	102
4.5	Numerical and experimental profiles of horizontal velocity on measurement line 1 at PL	104
4.6	Numerical and experimental profiles of horizontal velocity on measurement line 2 at PL	104
4.7	Deviation of numerical horizontal velocity data from experiment along measurement line 1 at PL	104
4.8	Contour plot of pressure distribution along the guide vanes at PL	105
4.9	Frequency spectrum of the numerical pressure signal at PL in vaneless space (VL2) obtained through FFT	107
4.10	Frequency spectrum of the numerical pressure signal at PL in draft tube cone (DT5) obtained through FFT	107
4.11	Frequency spectrum of the synchronous pressure fluctuations at PL obtained through FFT	108
4.12	Frequency spectrum of the asynchronous pressure fluctuations at PL obtained through FFT	108

4.13	Experimental and numerical axial velocity profiles on Lines 1 and 2. Solid lines represent simulation and dashed lines with square markers represent experiment	110
4.14	Experimental and numerical axial velocity profiles on Line 1 at a) BEP b) PL . Solid lines represent simulation and dashed lines with square markers represent experiment	113
4.15	Numerical horizontal (U) and normal (V) velocity profiles on Line 1	115
4.16	Numerical a) horizontal (U) and b) normal (V) velocity profiles on Line 1 at PL	116
4.17	Contours of normalized instantaneous axial velocity (W^*) in the draft tube at BEP and HL operating conditions	118
4.18	Contours of normalized instantaneous horizontal velocity (U^*) in the draft tube at BEP and HL operating conditions	119
4.19	Contours of normalized instantaneous normal velocity (V^*) in the draft tube at BEP and HL operating conditions	120
4.20	Contours of normalized instantaneous axial velocity (W^*) in the draft tube at BEP and PL operating conditions	122
4.21	Contours of normalized instantaneous horizontal velocity (U^*) in the draft tube at BEP and PL operating conditions	122
4.22	Contours of normalized instantaneous normal velocity (V^*) in the draft tube at BEP and PL operating conditions	123
4.23	Experimental and numerical axial velocity profiles on Line 1 at a) BEP b) HL	125
4.24	Experimental and numerical axial velocity profiles on Line 2 at a) BEP b) HL	125
4.25	Contours of normalized instantaneous axial velocity (W^*) in the draft tube at BEP and HL operating conditions obtained using PANS turbulence model	126
4.26	Contours of normalized instantaneous horizontal velocity (U^*) in the draft tube at BEP and HL operating conditions obtained using PANS turbulence model	127
4.27	Contours of normalized instantaneous normal velocity (V^*) in the draft tube at BEP and HL operating conditions obtained using PANS turbulence model	127
4.28	Cumulative energy of POD modes in velocity components on numerical plane over BEP, HL and PL operation	130
4.29	FFT of POD time coefficients under BEP operation	132
4.30	FFT of POD time coefficients under HL operation	133
4.31	FFT of POD time coefficients under PL operation	134
4.32	Contour plots of POD modes 2-5 of velocity components on numerical plane under BEP operation	137
4.33	Contour plots of POD modes 2-5 of velocity components on numerical plane under HL operation	138

4.34	Contour plots of POD modes 2-5 of velocity components on numerical plane under PL operation	139
5.1	Evolution of swirl number with time during BEP-HL transient operation	143
5.2	Evolution of swirl number with time during BEP-PL transient operation	144
5.3	Contour plots depicting spatiotemporal evolution of axial velocity (W^*) on Lines 1 and 2	147
5.4	Spatiotemporal evolution of axial velocity (W^*) on Line 1 [15].	147
5.5	Contour plot depicting spatiotemporal evolution of horizontal velocity (U^*) on Lines 1 and 2	149
5.6	Contour plot depicting spatiotemporal evolution of normal velocity (V^*) on Lines 1 and 2	149
5.7	Spatio-temporal contour plot of normalized axial velocity (W^*) on Line 1	153
5.8	Spatio-temporal contour plot of normalized horizontal velocity (U^*) on Line 1	156
5.9	Spatio-temporal contour plot of normalized normal velocity (V^*) on Line 1	156
5.10	Spatial contours of normalized axial velocity (W^*) in numerical plane at different time instants along transient operation	158
5.11	Spatial contours of normalized horizontal velocity (U^*) in numerical plane at different time instants along transient operation	159
5.12	Spatial contours of normalized normal velocity (V^*) in numerical plane at different time instants along transient operation	160
5.13	Variation of axial (W), horizontal (U) and normal (V) velocities at 5 points on Line 1 in the draft tube	163
5.14	Variation of axial (W), horizontal (U) and normal (V) velocities at 5 points on Line 2 in the draft tube	163
5.15	Evolution of normalized axial velocity (W^*) on Line 1	164
5.16	Evolution of normalized horizontal velocity (U^*) on Line 1	165
5.17	Evolution of normalized normal velocity (V^*) on Line 1	166
5.18	Contour plots of normalized axial velocity (W^*)	167
5.19	Contour plots of normalized horizontal velocity (U^*)	168
5.20	Contour plots of normalized normal velocity (V^*)	169
5.21	Temporal variation of static pressure in the vaneless space (VL2)	171
5.22	Fluctuation of pressure in the vaneless space (VL2)	173
5.23	Fluctuation of pressure near the wall of draft tube cone (DT5)	173
5.24	FFT of pressure fluctuations in vaneless space (VL2)	173
5.25	FFT of pressure fluctuations in draft tube cone (DT5)	174
5.26	Spectrogram of pressure fluctuations in vaneless space (VL2)	174
5.27	Spectrogram of pressure fluctuations in draft tube cone (VL2)	174

5.28	Radial distribution of averaged pressure in the draft tube. a) Line 1 and b) Line 2	175
5.29	Fluctuation of pressure a) vaneless space (VL2) b) draft tube (DT5) .	177
5.30	Spectrograms of pressure fluctuation obtained at a) vaneless space (VL2) b) draft tube (DT5)	178
5.31	Visuals of the iso surface of λ_2 at $750s^{-2}$ under BEP and HL operations	179
5.32	Streamlines of planar velocity (vp) across four radial cross-sections in the draft tube cone	180
5.33	λ_2 -iso-surfaces at $750s^{-2}$ within the draft tube at different time instants along HL – BEP transient operation	181
5.34	Streamlines of velocity (V_p) in xz (meridional) plane at different time instants along transient operation	183
5.35	λ_2 -iso-surfaces at $750s^{-2}$ within the draft tube at different time instants along BEP – PL transient operation	184
5.36	Streamlines of in-plane velocity on meridional xz plane in draft tube	185
5.37	Contour plots of magnitude of vorticity over BEP-HL load change . .	186
5.38	Contour plots of magnitude of vorticity over BEP-HL load change . .	188
5.39	Contour plots depicting spatiotemporal evolution of normalized axial velocity (W^*) on Line 1 obtained using PANS turbulence model . . .	189
5.40	Contour plots depicting spatiotemporal evolution of normalized horizontal velocity (U^*) on Line 1 obtained using PANS turbulence model	190
5.41	Contour plots depicting spatiotemporal evolution of non-dimensional normal velocity (V^*) on Line 1 obtained using PANS turbulence model	190
5.42	Spatial contours of normalized axial velocity (W^*) in numerical plane at different time instants obtained using PANS turbulence model . .	191
5.43	Spatial contours of normalized horizontal velocity (U^*) in numerical plane at different time instants obtained using PANS turbulence model	192
5.44	Spatial contours of normalized normal velocity (V^*) in numerical plane at different time instants obtained using PANS turbulence model	192
5.45	λ_2 -iso-surfaces at $750s^{-2}$ within the draft tube at different time instants along BEP – HL transient operation obtained using PANS turbulence model	193
5.46	Fluctuation of pressure in the vaneless space (VL2) predicted by PANS turbulence model	194
5.47	Fluctuation of pressure near the draft tube cone wall (DT5) predicted by PANS turbulence model	195
5.48	FFT of pressure fluctuation in the vaneless space (VL2) predicted by PANS turbulence model	195
5.49	FFT of pressure fluctuation near the draft tube cone wall (DT5) predicted by PANS turbulence model	195
5.50	Spectrogram of pressure fluctuation in the vaneless space (VL2) predicted by PANS turbulence model	196

5.51 Spectrogram of pressure fluctuation near the draft tube cone wall
(DT5) predicted by PANS turbulence model 196

List of Tables

3.1	Specifications of the test case under investigation	85
3.2	Mesh independency study[185]	91
3.3	Evaluation of grid discretization error based on GCI method	92
3.4	Mesh quality parameters	93
3.5	Simulated operating conditions	95
5.1	Comparison of computational resource for SAS and PANS simulations.	197

Abbreviations

AMI	A rbitrary M esh I nterface
APG	A dverse P ressure G radient
BEP	B est E fficiency P oint
CFD	C omputational F luid D ynamics
CRIO	C ompact R econfigurable I nput/ O utput
DNS	D irect N umerical S imulation
EVC	E nlarged V ortex C ore
GV	G uide V ane
HL	H igh L oad
HPC	H igh P erformance C omputer
IDC	I nnner C ore D iameter
LES	L arge E ddy S imulation
LEVM	L inear E ddy V iscosity M odel
Nd:YAG	N eodymium-doped Y ttrium A luminum G arnet
PISO	P ressure I mplicit with S plitting of O perator
PIV	P article I mage V elocimetry
PL	P art L oad
PVC	P recessing V ortex C ore
RANS	R eynolds- A veraged N avier- S tokes
RVR	R otating V ortex R ope
SIMPLE	S emi- I mplicit M ethod for P ressure- L inked E quations
URANS	U nsteady R eynolds- A veraged N avier- S tokes
VB	V ortex B reakdown

Symbols

f_n	Runner frequency (Hz)
k	Turbulent kinetic energy (J)
n_s	Specific speed (-)
I	Turbulence intensity
T_G	Generator torque
U	Horizontal component of velocity within numerical plane (m/s)
U_x	Velocity x -component (m/s)
U_y	Velocity y -component (m/s)
U_z	Velocity z -component (m/s)
U^*	Normalized horizontal component of velocity within numerical plane (-)
V^*	Normalized velocity component normal to numerical plane (-)
W	Axial component of velocity within numerical plane (m/s)
W^*	Normalized axial component of velocity within numerical plane (-)
x^*	Normalized radial distance from draft tube central axis
α	Guide vane angle ($^\circ$)
ϵ	Turbulence dissipation rate (m^2/s^3)
ν	Kinematic viscosity (m^2/s)
ν_t	Turbulent or eddy viscosity (m^2/s)
v_p	Planar velocity within central xz plane(m/s)
ω_{gv}	Guide vane angular speed ($^\circ/\text{s}$)